

Heavy quark structure functions from unifying the color dipole picture and double asymptotic scaling approaches

G.R.Boroun*

Department of Physics, Razi University, Kermanshah 67149, Iran
(Dated: February 13, 2024)

We present an analysis of the heavy quark structure functions from the k_t factorization scheme, using unifying the color dipole picture and double asymptotic scaling approaches at small x . The gluon distribution is obtained from the Golec-Biernat-Wüsthoff (GBW) and Bartels, Golec-Biernat and Kowalski (BGK) models. The main elements are based on the color dipole picture (CDP) and the generalized double asymptotic scaling (DAS) approach for usual parton distribution functions (PDFs). The comparisons with the HERA data are made and predictions for the proposed LHeC and FCC-he colliders are also provided in a wide range of the transverse separation r . In particular, the ratio $R^h = F_L^h/F_2^h$, $h = c, b, t$ is well described by the dipole models and is sensitive to the collider energies from HERA until FCC-he. We derive correlated bounds on the ratio F_2^c/F_2 and F_2^b/F_2 and compared them with the BGK and IP-sat models. The uncertainties are due to the renormalization and factorization scales at large and low r values. The Sudakov form factor into the heavy quark structure functions is incorporated and the results are considered, which are dependent on the hard scale in a wide range of the transverse separation r .

I. Introduction

The vector-meson-dominance (VMD) model [1,2] is an old idea that the scattering of a highly-energetic photon on a hadron may essentially be considered as a strong interaction process whenever a photon couples to hadrons it first converts to the vector mesons with universal coupling constants [3]. The VDM model was applied to deep inelastic scattering (DIS) on the assumption that the photon fluctuates into a series of vector mesons which subsequently scatter off the proton [4]. A similar idea, which is motivated to a large extent by perturbative quantum chromodynamics (pQCD), is the color dipole model (CDM) [5], which provides a successful description of deep inelastic scattering processes in a wide range of the kinematic variables [6]. The QCD color dipole formalism provides an intuitive description of inclusive and exclusive processes in electron-proton (ep) and lepton-nucleus (lA) scattering at high energies [7]. Although our knowledge of the proton structure at small- x is very limited, novel opportunities will be opened at new-generation facilities (Electron-Ion Collider(EIC), High-Luminosity Large Hadron Collider (HL-LHC), Forward Physics Facility (FPF)). Combining the information coming from dipole cross sections and p_T -unintegrated densities could play an important role. In particular, polarized amplitudes and cross sections for the exclusive electroproduction of ρ and ϕ mesons at the Hadron-Electron Ring Accelerator (HERA) and the EIC are very sensitive to the unintegrated gluon distribution (UGD) model adopted, whereas forward Drell-Yan dilepton distributions at the Large Hadron Collider beauty (LHCb) are very sensitive to next-to-leading logarithmic corrections.

In the color dipole picture (CDP) the absorption of a virtual photon on the proton $\gamma^* + p \rightarrow X$, is motivated by perturbation theory and describes photon-proton scattering as a two-step process. Firstly, the virtual photon dissociates into a quark-antiquark pair (a $q\bar{q}$ dipole) and subsequently the pair interacts with the proton, which is a purely hadronic reaction [8]. The CDP, at small x , gives a clear interpretation of the high-energy interactions, where is characterized by high gluon densities because the proton structure is dominated by dense gluon systems and predicts that the small x gluons in a hadron wavefunction should form a Color Glass Condensate [9,10].

In the high energy, $s \gg Q^2 \gg \Lambda_{QCD}^2$, regime these two processes are factorized, and the total cross section can be written as [5]

$$\sigma_{L,T}^{*p}(x, Q^2) = \int dz d^2\mathbf{r} |\Psi_{L,T}(\mathbf{r}, z, Q^2)|^2 \sigma_{\text{dip}}(x, \mathbf{r}), \quad (1)$$

*Electronic address: boroun@razi.ac.ir

where DIS cross section is factorized into a light-cone wave function and a dipole cross section. Indeed, the scattering between the virtual photon γ^* and the proton is seen as the color dipole where the transverse dipole size r and the longitudinal momentum fraction z with respect to the photon momentum are defined. The subscripts L and T referring to the transverse and longitudinal polarization state of the exchanged boson. Here $\Psi_{L,T}$ are the appropriate spin averaged light-cone wave functions of the photon and $\sigma_{\text{dip}}(x, r)$ is the dipole cross-section which related to the imaginary part of the $(q\bar{q})p$ forward scattering amplitude. The variable z , with $0 \leq z \leq 1$, characterizes the distribution of the momenta between quark and antiquark. The square of the photon wave function describes the probability for the occurrence of a $(q\bar{q})$ fluctuation of transverse size with respect to the photon polarization.

The key feature is the connection of the dipole cross section to the integrated gluon distribution. The parton saturation models shed light on the behavior of the gluon density at very low x and this knowledge is crucial for instance to describe the exclusive processes in ep and eA collisions [7]. The dipole cross section is related to the unintegrated gluon distribution [12]

$$\sigma(x, \mathbf{r}) = \frac{8\pi^2}{N_c} \int \frac{dk_t}{k_t^3} [1 - J_0(k_t \mathbf{r})] \alpha_s f(x, k_t^2), \quad (2)$$

where the integrated gluon distribution ($xg(x, \mu_r^2)$) is defined through the unintegrated gluon distribution ($f(x, k_t^2)$) by

$$xg(x, \mu_r^2) \equiv \int^{\mu_r^2} \frac{dk_t^2}{k_t^2} f(x, k_t^2). \quad (3)$$

Indeed, the dipole cross section is directly connected via a Fourier transform to the small- x UGD, whose evolution in x is regulated by the Balitsky- Fadin-Kuraev-Lipatov (BFKL) equation [13]. Single and double BFKL pomeron exchanges have been calculated by illustrating a dipole picture of high energy hard scattering in the large N_c limit in the leading logarithmic approximation in Ref.[14].

The BFKL equation governs the evolution of the UGD, where the k_T -factorization is used in the high energy limit in which the QCD interaction is described in terms of the quantity which depends on the transverse momentum of the gluon. The gluon density in inclusive and exclusive processes in a wide Q^2 region at low x is desirable, in the dominant double logarithmic (DLA) contribution by the following form [15]

$$xg(x, \mu_r^2) \propto \exp \left[\frac{16N_c}{\beta_0} \ln \frac{x_0}{x} \ln \frac{t}{t_0} \right], \quad (4)$$

where $\frac{t}{t_0} \equiv \ln(\frac{\mu_r^2}{\Lambda_{QCD}^2}) / \ln(\frac{Q_0^2}{\Lambda_{QCD}^2})$ and $\beta_0 = 11 - \frac{2}{3}n_f$. Here n_f is the number of active flavours. The hard scale μ_r is assumed to have the form $\mu_r^2 = C/r^2 + \mu_0^2$ where the parameters C and μ_0 are obtained from the fit to the DIS data. A matching between the dipole model gluon distribution and the collinear approach, in the improved saturation model, is obtained [15,16] by using a leading order gluon anomalous dimension γ_{gg} as

$$xg(x, \mu_r^2) \propto I_0 \left(2 \sqrt{\frac{12}{\beta_0} \ln \frac{x_0}{x} \ln \frac{t}{t_0}} \right) \exp \left[-\delta \ln \frac{t}{t_0} \right], \quad (5)$$

where $\delta = (11 + \frac{2n_f}{27})/\beta_0$.

A novel formulation of the UGD for DIS in a way that accounts for the leading powers in both the Regge and Bjorken limits is presented in Ref.[17]. In this way, the UGD is defined by an explicit dependence on the longitudinal momentum fraction x which entirely spans both the dipole operator and the gluonic Parton Distribution Function. The object of the BFKL evolution equation at very small x is the differential gluon structure function of proton

$$f(x, k_t^2) = \frac{\partial[xg(x, \mu_r^2)]}{\partial \ln \mu_r^2} \Big|_{\mu_r^2 = k_t^2} \quad (6)$$

which emerges in the color dipole picture (CDP) of inclusive deep inelastic scattering (DIS) and diffractive DIS into dijets [18]. Here x and k_t^2 being the fractional momentum of proton carried by gluon and the transverse momentum of gluon respectively. Unintegrated distributions are required to describe measurements where transverse momenta are exposed explicitly. Eq.(6) cannot remain true as x increases or decreases [19], therefore modify Eq.(6), with the

Sudakov form factor, to the form ¹ [21]

$$f(x, k_t^2) = \frac{\partial[xg(x, \mu_r^2)T(r, \mu_r^2)]}{\partial \ln \mu_r^2} \Big|_{\mu_r^2 = k_t^2}, \quad (7)$$

with $T(r, \mu_r^2) = \exp(-S(r, \mu_r^2))$ where the perturbative Sudakov factor in the leading-order [22], for the case of running coupling $\alpha_s(\mu_r^2) = 1/(b_0 \ln \frac{\mu_r^2}{\Lambda_{\text{QCD}}^2})$, reads

$$S_{\text{pert}}^{(1)}(r, Q^2) = \frac{C_A}{2\pi b_0} \left[-\ln \left(\frac{Q^2}{\mu_b^2} \right) + \left(\frac{1 + \alpha_s(\mu_b^2)b_0 \ln \left(\frac{Q^2}{\mu_b^2} \right)}{\alpha_s(\mu_b^2)b_0} \right) \ln \left(1 + \alpha_s(\mu_b^2)b_0 \ln \left(\frac{Q^2}{\mu_b^2} \right) \right) \right], \quad (8)$$

where $b_0 = \frac{11C_A - 2n_f}{12}$ and $\mu_b = 2e^{-\gamma_E}/r$ where $\gamma_E \approx 0.577$ is the Euler-Mascheroni constant.

The proton structure function F_2 corresponds to the dipole picture of DIS at small x , by Eq.(1), as

$$F_2 = F_T + F_L = \frac{Q^2}{4\pi^2 \alpha_{em}} \left(\sigma_T^{\gamma^* p} + \sigma_L^{\gamma^* p} \right). \quad (9)$$

Since the photon wave function depends on mass of the quarks in the color dipole model [23], then the light and heavy structure functions are defined by the following form

$$F_{T,L} = F_{T,L}^l + F_{T,L}^h, \quad (10)$$

where $F_{T,L}^l$ is the sum of the contributions from the light quark pairs, while $F_{T,L}^h$ is the contribution from the heavy quarks ($c\bar{c}$, $b\bar{b}$ and may be $t\bar{t}$). So the Bjorken variable x can be modified in the gluon distribution and dipole cross section by the following form

$$x \rightarrow \tilde{x}_f = \frac{Q^2 + 4m_f^2}{Q^2 + W^2}, \quad (11)$$

where W^2 is an invariant energy squared of the $\gamma^* p$ system and m_f is the mass of the quark of flavour f .

Heavy-quarks production, in neutral current (NC) deep inelastic electron-proton scattering (DIS) at HERA, is the most important quantum chromodynamics (QCD) tests. The production of heavy quarks at HERA depends on the mass of these quarks and thus the calculations of cross sections depend on a wide range of perturbative scales μ^2 . The massive fixed-flavour-number scheme (FFNS) [25] and the variable-flavour-number scheme (VFNS) [26] are different approaches for considering heavy quarks. FFNS can be used on the threshold of $\mu^2 \approx m_f^2$ and for $\mu^2 \gg m_f^2$ VFNS is used where the treatment of resummation of collinear logarithms $\ln(\mu^2/m_f^2)$ is achieved. A general-mass variable-flavour-number scheme (GM-VFNS) for calculation of the contributions of heavy quarks introduced in Ref.[27]. For realistic kinematics it has to be extended to the case of a GM-VFNS which is defined similarly to the zero-mass VFNS (ZM-VFNS) in the $Q^2/m_f^2 \rightarrow \infty$ limit [28]. In GM-VFNS the transition, from n_f active flavors to $n_f + 1$, is considered in the construction of the charm-quark parton distribution function. At some rather large scales (i.e., $Q^2 > m_f^2$) the transition to two massive quarks (i.e., $n_f \rightarrow n_f + 2$) has been discussed in Refs.[29,30]. In the GM-VFNS at high Q^2 , the heavy-flavor structure functions depend on the active flavor number since here $n_f = 4$ for $m_c^2 < \mu^2 < m_b^2$, $n_f = 5$ for $m_b^2 < \mu^2 < m_t^2$ and $n_f = 6$ for $\mu^2 \geq m_t^2$ is chosen.

The dynamics of flavor-singlet quark and gluon distribution functions, q^s and g , are defined by

$$\begin{aligned} q^s(x, n_f, \mu^2) &= \sum_{l=1}^{n_f} [f_l(x, n_f, \mu^2) + \bar{f}_l(x, n_f, \mu^2)], \\ g(x, n_f, \mu^2) &= f_g(x, n_f, \mu^2). \end{aligned} \quad (12)$$

¹ The Sudakov form factor can be defined into the dipole models with the help of the following formula [20] :

$$\sigma_{\text{dip}}(x, r, Q^2) = \int_0^r dr' r' \log\left(\frac{r}{r'}\right) e^{-S(r', Q^2)} \nabla_{r'}^2 \sigma_{\text{dip}}(x, r')$$

² The high ep cms energy at the LHeC will lead to the copious production of single top-quarks, about 2×10^6 single top and 5×10^4 $t\bar{t}$ events [24].

The heavy-quark structure functions derived using the zero-mass VFN scheme (ZMVFN) by the following form

$$F_k^{ZMVFN} = \sum_{j=0}^{\infty} a_s^j(n_f + 1) \sum_{i=q,g,h} C_{k,i}^{(j)}(n_f + 1) \otimes f_i(n_f + 1) \quad (13)$$

where C 's are the Wilson coefficients at the j -th order and $k = 2$ and L and the \otimes symbol denotes the convolution integral which turns into a simple multiplication in Mellin N -space. The notation is defined by $a(x) \otimes b(x) = \int_x^1 \frac{dz}{z} a(z) b(\frac{x}{z})$. Here $a_s = \frac{\alpha_s}{4\pi}$ is the QCD running coupling. Eq.(13), at asymptotically large momentum transfer $Q^2 \gg m_f^2$, is valid. For $Q^2 \simeq m_f^2$ VFNS is valid which it includes a combination of the ZMVFN with FFNS. In this case the heavy-quark structure functions are

$$F_k^{FFNS} = \sum_{j=0}^{\infty} a_s^j(n_f) \sum_{i=q,g} H_{k,i}^{(j)}(n_f) \otimes f_i(n_f), \quad (14)$$

where H 's are the Wilson coefficients for the DIS heavy-quark production [30].

In this paper we present the heavy quark structure functions due to the dipole models in the collinear approach. These calculations are based on the generalized double asymptotic scaling (DAS) approach [31-34]. We continue our investigations and analyze the heavy quark structure functions and those ratios in a wide range of r in section II. In this section, the heavy quark structure functions can be combined with the Sudakov form factor. Sections III and IV contains our results and conclusions respectively.

II. Method

• Structure Functions :

The heavy quark structure functions in DIS in ep colliders are obtained from the measurements of the inclusive heavy quark cross sections, which will be an important test of the QCD in the LHeC and FCC-he colliders [24]. The reduced cross section of the top quark is defined in terms of the top structure functions by the following form:

$$\sigma_{\text{red}}^{h\bar{h}}(x, Q^2) = \frac{xQ^4}{2\pi\alpha_{EM}^2[(1 + (1 - y)^2)]} \frac{d^2\sigma^{h\bar{h}}}{dx dQ^2} = F_2^h(x, Q^2) - f(y)F_L^h(x, Q^2), \quad (15)$$

where $f(y) = \frac{y^2}{1 + (1 - y)^2}$. In HERA kinematic range the contribution $F_L^{h\bar{h}}$ is small. Therefore the heavy-quark structure function F_2^h is obtained from the measured heavy-quark cross sections. The ratio $R^h(x, Q^2) = F_L^h(x, Q^2)/F_2^h(x, Q^2)$ will extend in future circular colliders (i.e., LHeC and FCC-he). Indeed, these new colliders are the ideal place to resolve this ratio.

In the small x range, where the gluon contribution is dominant, the heavy quark structure functions in the collinear generalized DAS approach are given by [34]

$$F_k^h(x, \mu_r^2) \simeq e_h^2 \sum_{n=0}^{\infty} \left(\frac{\alpha_s}{4\pi}\right)^{n+1} B_{k,g}^{(n)}(x, \xi_r) \otimes xg(x, \mu_r^2), \quad (16)$$

where $B_{k,g}$ are the collinear Wilson coefficient functions in the high energy regime [34] and e_h^2 is the squared charge of the heavy flavor. Here, n denotes the order in running coupling α_s and $\xi_r = \frac{m_f^2}{\mu_r^2}$. The explicit expressions for the coefficient functions at the leading order (LO) up to next-to-next-to-leading order (NNLO) approximations are relegated in Appendix. The default renormalisation and factorization scales are set to be equal $\mu_R^2 = \mu_r^2 + 4m_f^2$ and $\mu_F^2 = \mu_r^2$.

The integrated and unintegrated gluon distributions from the GBW and BGK models are obtained in Ref.[35], which were formulated on the position-space version of the k_t -factorization formula. The gluon density is parametrized at the scale μ_r^2 using the running coupling α_s by the following form

$$xg(x, \mu_r^2) = \frac{\sigma_0}{16\pi^3} Q_0^2 \left(\frac{x_0}{x}\right)^\lambda (11C_A - 2n_f) \ln\left(\frac{\mu_r^2}{\Lambda_{QCD}^2}\right). \quad (17)$$

TABLE I: The fixed parameters according to Ref.[23] from the fit results to the HERA data using the dipole cross section.

Ref.	m_l [GeV]	m_c [GeV]	m_b [GeV]	σ_0 [mb]	λ	$x_0/10^{-4}$	χ^2/N_{dof}
[23]	0.14	1.4	-	27.32 ± 0.35	0.248 ± 0.002	0.42 ± 0.04	1.60
[23]	0.14	1.4	4.6	27.43 ± 0.35	0.248 ± 0.002	0.40 ± 0.04	1.61

where $C_A = N_c = 3$ is the Casimir operator in the fundamental and adjoint representation of the $SU(N_c)$ color group and the QCD parameter Λ is extracted by $\alpha_s(M_Z^2)$ using the c and b-quark threshold³.

The parameters of the model (i.e., σ_0 , x_0 and λ) depend on the active flavor number are found from a fit to small- x data in Table I. After exploiting the low x behavior of the gluon density (i.e., Eq.(17)), Eq.(16) can be rewritten as

$$F_k^h(x, \mu_r^2) \simeq M_{k,g}^h(x, \mu_r^2, \lambda) x g(x, \mu_r^2) \quad (18)$$

where

$$M_{k,g}^h(x, \mu_r^2, \lambda) = e_h^2 \sum_{n=0} \left(\frac{\alpha_s}{4\pi} \right)^{n+1} \int_x^{x_2} B_{k,g}^{(n)}(y, \xi_r) y^{\lambda-1} dy. \quad (19)$$

Therefore, the explicit form of the heavy structure functions at the LO approximation, in the particular case of off-shell initial gluons (when $k^2 = 0$) is

$$\begin{aligned} F_2^h(x, \mu_r^2) &= e_h^2 \frac{3\sigma_0}{16\pi^3} Q_0^2\left(\frac{x_0}{x}\right)^\lambda \int_x^{x_2} \left\{ -2y\beta \left[1 - 4y(2 - \xi_r)(1 - y) - \left(1 - 2y(1 - 2\xi_r) \right. \right. \right. \\ &\quad \left. \left. \left. + 2y^2(1 - 6\xi_r - 4\xi_r^2) \right) L(\beta) \right] \right\} y^{\lambda-1} dy, \\ F_L^h(x, \mu_r^2) &= e_h^2 \frac{3\sigma_0}{16\pi^3} Q_0^2\left(\frac{x_0}{x}\right)^\lambda \int_x^{x_2} 8y^2\beta \left[(1 - y) - 2y\xi_r L(\beta) \right] y^{\lambda-1} dy, \end{aligned} \quad (20)$$

where $\beta = \sqrt{1 - \frac{4x\xi_r}{1-x}}$ and $L(\beta) = \frac{1}{\beta} \ln \frac{1+\beta}{1-\beta}$. The ratio $R^h(x, \mu_r^2) = \frac{F_L^h(x, \mu_r^2)}{F_2^h(x, \mu_r^2)}$ can be presented as

$$\begin{aligned} R^h(x, \mu_r^2) &= \frac{M_{L,g}(x, \mu_r^2, \lambda)}{M_{2,g}(x, \mu_r^2, \lambda)} \\ &= \frac{\int_x^{x_2} 8y^2\beta [(1 - y) - 2y\xi_r L(\beta)] y^{\lambda-1} dy}{\int_x^{x_2} \{ -2y\beta [1 - 4y(2 - \xi_r)(1 - y) - (1 - 2y(1 - 2\xi_r) + 2y^2(1 - 6\xi_r - 4\xi_r^2)) L(\beta)] \} y^{\lambda-1} dy} \end{aligned} \quad (21)$$

where the ratio is independent of the gluon density, the Sudakov form factor and the running coupling at the LO approximation. The Sudakov form factor can be included by using Eq.(8) and generalizing it to the heavy quark structure functions (i.e., Eq.(18)) by the following form

$$F_k^h(x, \mu_r^2) = e^{-S(r, \mu_r^2)} M_{k,g}^h(x, \mu_r^2, \lambda) x g(x, \mu_r^2) \quad (22)$$

The heavy quark structure functions now depend on the non-linear gluon evolution at small x due to the Sudakov effects, which become relevant for processes with two distinct scales.

• Bounds :

In the following, we discuss further bounds [7, 38-41] for F_2^c/F_2 and F_2^b/F_2 which follow from the standard dipole picture. Indeed, we give correlated bounds for $F_2^{c,b}/F_2$ versus F_L/F_2 where the higher Fock components of the photon

³ In Refs.[36] and [37], the massive quarks in NLO dipole factorization for DIS are considered. The NLO corrections for the dipole factorization of DIS structure functions at low x is considered using light front perturbative theory as

$$|\gamma_{T,L}^* >_{NLO} = |\gamma_{T,L}^* >_{q\bar{q}} + |\gamma_{T,L}^* >_{q\bar{q}g}.$$

wave function affect these bounds. In Refs.[38,39], the authors have shown that the upper bound is independent of Q^2 and numerically leads to $\frac{F_L(W,Q^2)}{F_2(W,Q^2)} \leq g_{\max} = 0.27139$ for the case of massless quarks. A stronger bound can be obtained by considering the effect of the charm and bottom quarks on the ratio

$$\frac{F_L^{\text{light+c+b}}}{F_2^{\text{light+c+b}}} = \frac{F_L + F_L^c + F_L^b}{F_2 + F_2^c + F_2^b} = \frac{F_L/F_2 + F_L^c/F_2^c F_2^c/F_2 + F_L^b/F_2^b F_2^b/F_2}{1 + F_2^c/F_2 + F_2^b/F_2} \leq g_{\max} \frac{1 + g_{\max}^c F_2^c/F_2 + g_{\max}^b F_2^b/F_2}{1 + F_2^c/F_2 + F_2^b/F_2} \leq g_{\max} \quad (23)$$

In this case the bound on the ratio F_L/F_2 will depend on the values of F_2^c/F_2 and F_2^b/F_2 , where these bounds (i.e., F_2^h/F_2) can further restrict the kinematical range of applicability of the dipole picture in future colliders [24,42]. In the CDP, the gluon distribution has been recently determined in Ref.[43] at low x by the following form

$$\alpha_s(\mu_r^2) x g(x, \mu_r^2) = \frac{9\pi}{R_{e^+e^-}} \frac{1}{2\rho + 1} F_2(\eta_L x, \mu_r^2), \quad (24)$$

where $R_{e^+e^-} = N_c \sum_f e_f^2$ and $\eta_L \simeq 0.40$ is the rescaling factor. The ρ parameter describes the ratio of the average transverse momenta $\rho = \frac{\langle \vec{k}_\perp^2 \rangle_L}{\langle \vec{k}_\perp^2 \rangle_T}$, which the transverse momentum \vec{k}_\perp^2 is introduced into four momenta of the quark and antiquark. The quantity of ρ , for $Q^2 \gg \Lambda_{\text{sat}}^2$, was used to be $\rho = 4/3$ [44]. The ratio of the longitudinal to the transversal photoabsorption cross sections is given by

$$R = \frac{\sigma_L^{\gamma^* p}}{\sigma_T^{\gamma^* p}} = \frac{1}{2\rho}, \quad (25)$$

where factor 2 originates from the difference in the photon wave functions. In terms of the proton structure functions, F_2 and F_L , the ratio becomes⁴

$$\frac{F_L}{F_2} = \frac{1}{1 + 2\rho}. \quad (26)$$

With imposing consistency between the CDP and the pQCD, the gluon distribution function is obtained by expressing the proton structure function in terms of F_L as

$$\alpha_s(\mu_r^2) x g(x, \mu_r^2) = \frac{3\pi}{\sum_f e_f^2} F_L(\eta_L x, \mu_r^2). \quad (27)$$

Therefore the ratio F_2^h/F_2 and F_L^h/F_L are defined by

$$\frac{F_2^h}{F_2} = \frac{3}{4} \frac{e_h^2}{\eta_L^\lambda \sum_f e_f^2} \frac{\int_x^{x_2} B_{2,g}^{(0)}(y, \xi_r) y^{\lambda-1} dy}{2\rho + 1} \quad (28)$$

and

$$\frac{F_L^h}{F_L} = \frac{3}{4} \frac{e_h^2}{\eta_L^\lambda \sum_f e_f^2} \int_x^{x_2} B_{L,g}^{(0)}(y, \xi_r) y^{\lambda-1} dy. \quad (29)$$

These ratios are very interesting in the range of available HERA energy and its extension to future energies in LHeC and FCC-he colliders.

⁴ The colored sector of the virtual photon wave-functions contains both $q\bar{q}$ and $q\bar{q}g$ components at the NLO approximation. Expansion of the structure functions, F_2 and F_L , in Fock state in the CDM are given by

$$F_{2,L} = F_{2,L}^{q\bar{q}} + F_{2,L}^{q\bar{q}g} + \dots$$

where at higher Fock states one can be derived [37] the modified CDM bound for the ratio $\frac{F_L}{F_2}$ as

$$\left(\frac{F_L}{F_2} \right)_{\text{NLO}} = \left(\frac{F_L}{F_2} \right)_{\text{LO}} \frac{1 + \delta\epsilon}{1 + \epsilon}$$

where $\epsilon = \frac{F_2^{q\bar{q}g}}{F_2^{q\bar{q}}}$ and $0 \leq \delta \leq 3.7$.

III. Numerical Results

In the present paper we consider the heavy quark structure functions to the deep inelastic proton structure function, which are directly related with the gluon distribution of the proton in the CDP approach at low x . Everywhere below, we set the charm and bottom masses to be equal to $m_c = 1.4$ GeV and $m_b = 4.6$ GeV according to Ref.[23]. In accordance with the values recommended by the Higgs Cross Section Working Group [45], the top-quark pole mass is set as in the NNPDF default analysis to $m_t = 172.5$ GeV [46]. To estimate the scale uncertainties of our calculations, the standard variations in default renormalization and factorization scales, which were set to be equal to $\mu_R^2 = \mu_r^2 + 4m^2$ and $\mu_F^2 = \mu_r^2$, respectively, were introduced. In recent years [47,48], the phenomenological various

TABLE II: The transverse separation range of r in the HERA and future colliders (i.e., LHeC and FCC-he) with the inelasticity $y \leq 1$ for $x = 0.0013$ and 0.0050 .

Collider	\sqrt{s} [GeV]	$x=0.0013$	$x=0.0050$
FCC-he	3500	$r > 0.005$	$r > 0.002$
LHeC	1300	$r > 0.01$	$r > 0.006$
HERA	320	$r > 0.05$	$r > 0.02$

successful methods have examined charm and bottom structure functions. This importance, along with the t-quark density [49,50], can be explored at future circular collider energies.

Our numerical results for charm and bottom structure functions, F_2^c and F_2^b , are shown in Figs.1 and 2, respectively,

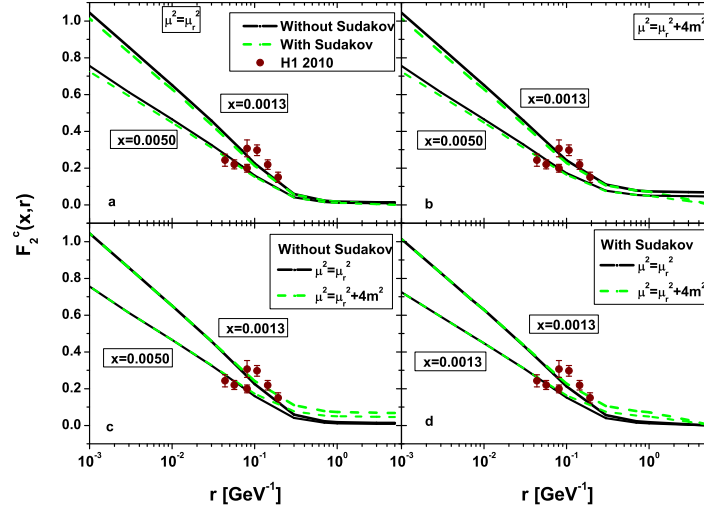


FIG. 1: Comparison of the H1 data from [51] for the charm F_2^c structure function with the results from unifying the color dipole picture and double asymptotic scaling approaches with the parameters in Table I in a wide range of the transverse separation r [GeV $^{-1}$]. The uncertainties are due to $\mu^2 = \mu_r^2 + 4m^2$, $\mu^2 = \mu_r^2$ and the Sudakov form factor with $x = 0.0013$ and 0.0050 .

in comparison with the H1 data [51]. To estimate the uncertainties of our calculations, the standard variations in default scales (i.e., renormalization and factorization) and the behavior of the Sudakov form factor are introduced. We observe that the predictions obtained using unifying the color dipole picture and double asymptotic scaling approaches in a proton are in perfect agreement with the H1 data in a wide range of r for $x = 0.0013$ and 0.0050 within the total experimental uncertainties. These results for F_2^c and F_2^b , in Figs.1 and 2, increase as r decreases. As a result, we predict that at very low r , the charm and bottom structure functions will increase at the FCC-he than the LHeC and HERA at high inelasticity according to Table II. The uncertainties (without and with Sudakov effects) increase as r increase. In Fig.1-c,d, we observe that the uncertainties for the charm structure functions increase for $r \gtrsim 2 \times 10^{-1}$ GeV $^{-1}$ and for the bottom structure functions increase for $r \gtrsim 3 \times 10^{-2}$ GeV $^{-1}$ in Fig.2-c,d. The effect

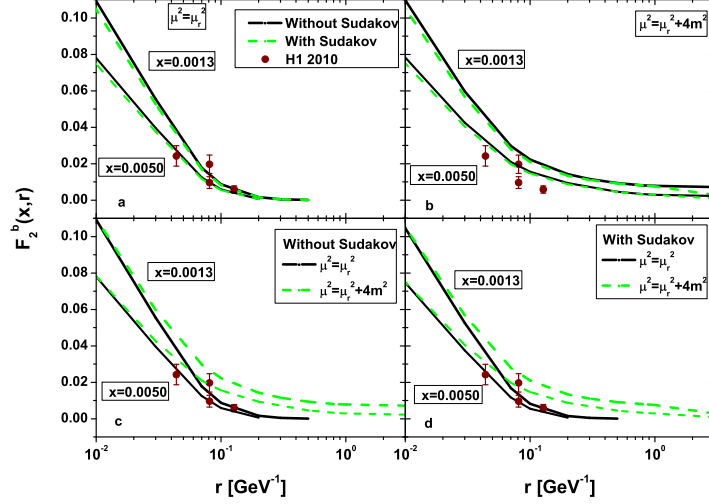


FIG. 2: The same as Fig.1 for the bottom structure function.

of the Sudakov form factors in the charm and bottom structure functions are shown in Figs.1-a,b and 2-a,b for the renormalization and factorization scales, respectively. Differences between the results (with and without Sudakov form factor) for the charm and bottom structure functions are very small and visible at small r . One can see that the Sudakov factor mostly disappears in the large- r region for $\mu^2 = \mu_r^2$ and survives for $\mu^2 = \mu_r^2 + 4m^2$ at $r > 2 \text{ GeV}^{-1}$. The changes are less obvious compared to the charm and bottom structure functions without Sudakov form factor, which is because the large- r region, where the dipole cross section was affected the most, is largely suppressed by the photon wave function. In conclusion, the structure functions with Sudakov form factor seem to show slightly more change in a wide range of r . We can add these results as associated with the LHeC simulated uncertainties [24]. These simulated uncertainties for F_2^c and F_2^b measurements were recently published by the LHeC study group and reported by Ref.[24]⁵.

In Figs.3 and 4, the importance of the longitudinal structure function for charm and bottom pair production, F_L^c and F_L^b , are examined according to Table II for colliders (HERA, LHeC and FCC-he) in a wide range of r . The behavior of these structure functions considers with and without Sudakov form factor in a wide range of r for $x = 0.0013$ and 0.0050 in Figs.3 and 4. In Fig.3-c,d, we observe that the uncertainties for the F_L^c increase for $r \gtrsim 10^{-1} \text{ GeV}^{-1}$ and for the F_L^b increase for $r \gtrsim 5 \times 10^{-2} \text{ GeV}^{-1}$ in Fig.4-c,d. The effect of the Sudakov form factors in the F_L^c and F_L^b are shown in Figs.13-a,b and 4-a,b for the renormalization and factorization scales, respectively. Differences between the results (with and without Sudakov form factor) are very small and visible at small r . One can see that the Sudakov factor mostly disappears in the large- r region for $\mu^2 = \mu_r^2$ and survives for $\mu^2 = \mu_r^2 + 4m^2$ at $r > 2 \text{ GeV}^{-1}$. According to Figs.3 and 4, we observe that the longitudinal structure function for charm and bottom increase as r decreases due to the HERA range of r (see Table II). We observe that the F_L^c and F_L^b in the LHeC and FCC-he range energy makes the transition from the large r to the low r forms. The longitudinal structure functions for charm ($r \gtrsim 3 \times 10^{-1} \text{ GeV}^{-1}$) and bottom ($r \gtrsim 10^{-1} \text{ GeV}^{-1}$) are slowly varying and reach to zero for large r . These values have a constant rate at lower r . The ratio of the longitudinal structure functions, $\frac{F_L^c}{F_L^b}$, is of the $\mathcal{O}(\frac{m_b}{m_c})$ order for $r < 10^{-2} \text{ GeV}^{-1}$. This ratio shows that the importance of measuring the longitudinal structure function for bottom quark is not less than charm quark in the process analysis of new colliders.

Considering the top structure function in unifying the color dipole picture and double asymptotic scaling approaches is interesting because the production of top quarks in electron-proton collisions at LHeC and FCC-he can provide a stringent test of new physics at ultra-high energy (UHE). In Fig.5, the top structure function is predicted in a wide range of the transverse separation range of r with $\mu^2 = \mu_r^2 + 4m^2$ for $x = 0.0013$. The Sudakov form factor effect is

⁵ For further discussion, such predictions can be found in Figs. 3.4, 3.6 and 3.7 of Ref.[24].

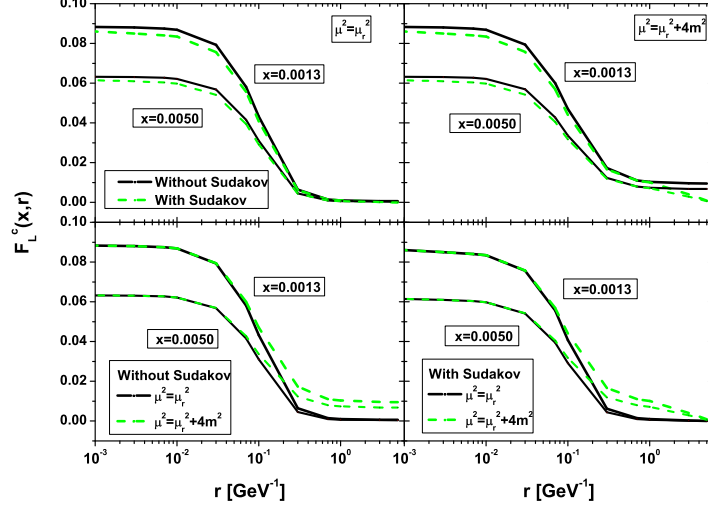


FIG. 3: The behavior of the charm F_L^c structure function due to unifying the color dipole picture and double asymptotic scaling approaches with the parameters in Table I in a wide range of the transverse separation r [GeV^{-1}]. The uncertainties are due to $\mu^2 = \mu_r^2 + 4m^2$, $\mu^2 = \mu_r^2$ and the Sudakov form factor with $x = 0.0013$ and 0.0050 .

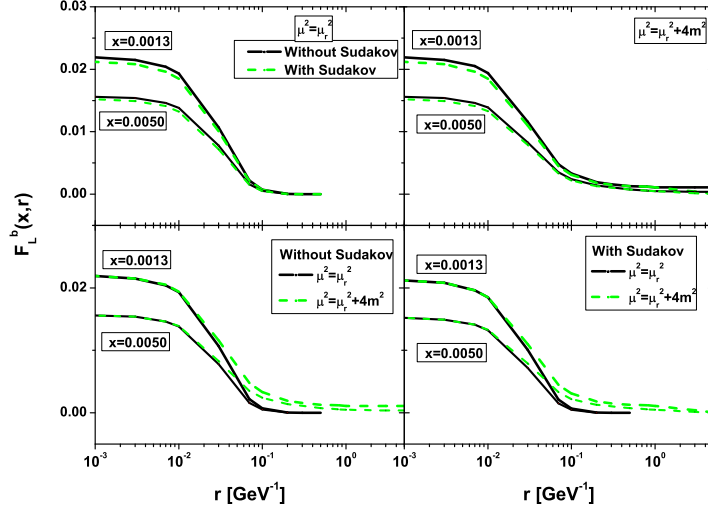


FIG. 4: The same as Fig.3 for the bottom structure function.

compared with these results in Fig.5. The difference between the results (with and without Sudakov form factor) for the top structure function is very small and visible at small r . One can see that the Sudakov factor mostly disappears in the large- r region. It is observed that in the HERA energy range ($r \gtrsim 0.05 \text{ GeV}^{-1}$), the top structure function is zero. This probability increases as the energy range increases to future colliders (especially FCC-he). It is clear that the top structure function will increase at the FCC-he than the LHeC at high inelasticity⁶, according to Table II. It

⁶ Notice that the large inelasticity is only for scattered electron energies much smaller than the electron beam energy (i.e., $E_e' \ll E_e$ and $y = 1 - E_e'/E_e$). In this region where E_e' is small, the electromagnetic and hadronic backgrounds are important [24].

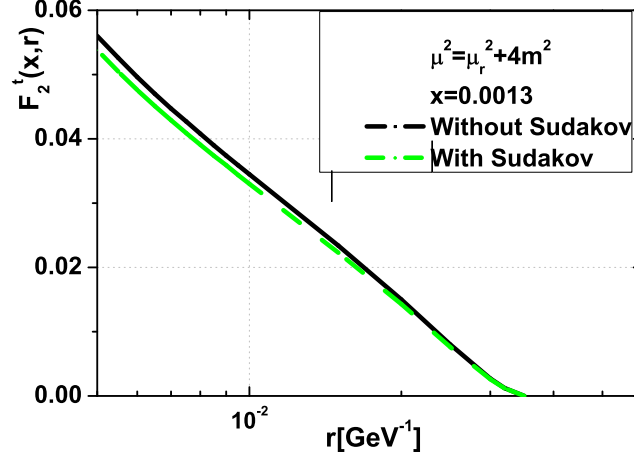


FIG. 5: Results of the top F_2^t structure function with the bottom parameters in Table I in a wide range of the transverse separation r [GeV^{-1}] at $\mu^2 = \mu_r^2 + 4m^2$ with and without Sudakov form factor for $x = 0.0013$.

reaches $F_2^t \simeq 0.05$ at $r \simeq 0.005 \text{ GeV}^{-1}$ in the FCC-he energy range and $F_2^t \simeq 0.03$ at $r \simeq 0.01 \text{ GeV}^{-1}$ in the LHeC energy range for $x = 0.0013$ with $\mu^2 = \mu_r^2 + 4m^2$.

Results of our calculations for $R^c = \frac{F_2^c}{F_2^t}$ and $R^b = \frac{F_2^b}{F_2^t}$ are presented in Fig.6 and 7 respectively, where we plot these

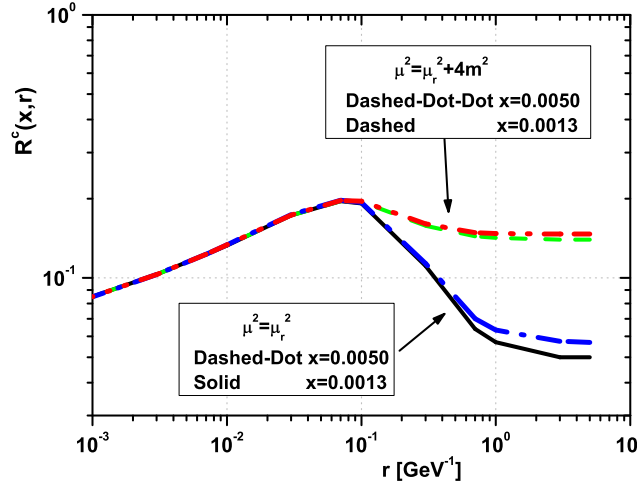


FIG. 6: R^c evaluated as a function of r with $\mu^2 = \mu_r^2$ and $\mu^2 = \mu_r^2 + 4m^2$ for $x = 0.0013$ and 0.0050 .

ratios as a function of x in a wide r range with $\mu^2 = \mu_r^2$ and $\mu^2 = \mu_r^2 + 4m^2$. We observe from Figs.6 and 7 that these results for $r \gtrsim 10^{-1} \text{ GeV}^{-1}$ leads to a flat behavior of R^c and R^b with $\mu^2 = \mu_r^2 + 4m^2$ and decrease sharply with $\mu^2 = \mu_r^2$. The results obtained with the renormalization and factorization scales for R^c and R^b are compatible at $r < 10^{-1} \text{ GeV}^{-1}$ and $3 \times 10^{-2} \text{ GeV}^{-1}$ respectively and have the largest uncertainties at $r > 10^{-1} \text{ GeV}^{-1}$ and $3 \times 10^{-2} \text{ GeV}^{-1}$. Our calculations show an x -independent behavior of R^c and R^b in a wide range of r with the renormalization and factorization scales. For larger values of r , some dependence on x appears, especially in R^c with $\mu^2 = \mu_r^2$ and in R^b with $\mu^2 = \mu_r^2 + 4m^2$. The maximum value of $R(x, r)$ is equal to $\simeq 0.2$ for charm and bottom ratios at $r \simeq 10^{-1} \text{ GeV}^{-1}$ and $3 \times 10^{-2} \text{ GeV}^{-1}$ respectively. We observe that the maximum value shifts to smaller values of

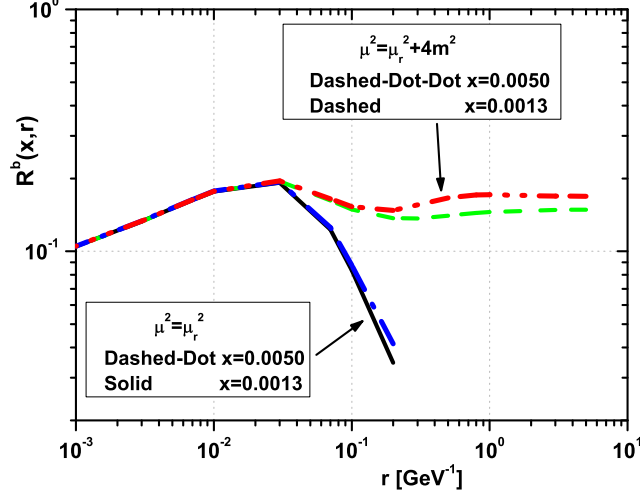


FIG. 7: The same as Fig.5 for the ratio of the bottom structure functions R^b .

r for the bottom quark than the charm. These results are comparable with others in literature [24, 31, 32, 34, 52]. In order to assess the significance of the ratio of structure functions in a wide range of the collider energies (from

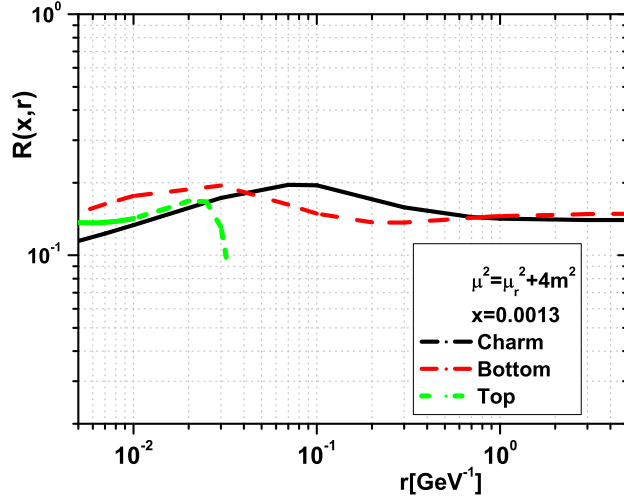


FIG. 8: R^c , R^b and R^t evaluated as a function of r with $\mu^2 = \mu_r^2 + 4m^2$ for $x = 0.0013$.

HERA until FCC-he), we show in Fig.8 the r dependences of R^c , R^b and R^t evaluated with $\mu^2 = \mu_r^2 + 4m^2$ for $x = 0.0013$. We observe from Fig.8 that the charm and bottom predictions have similar behaviors in a wide range of r and collider energies (according to Table II). The charm and bottom ratios increase until $r \simeq 10^{-1} \text{ GeV}^{-1}$ and $3 \times 10^{-2} \text{ GeV}^{-1}$ respectively, then decrease and have a flat (r -independent) behavior for large values of r ($r \geq 0.3 \text{ GeV}^{-1}$). In Fig.8, we observe the ratio of the top structure functions according to the FCC-he center-of-mass energy in the inelasticity range $0 < y < 1$ due to the coefficients in Table I. It continues to rise with r , then fall

after reaching a maximum⁷. Such results seem to be extremely important for future experiments, in particular, for experiments at the LHeC and FCC-he.

In Fig.9, we plot ratios F_2^c/F_2 and F_2^b/F_2 as functions of r with the renormalization and factorization scales for

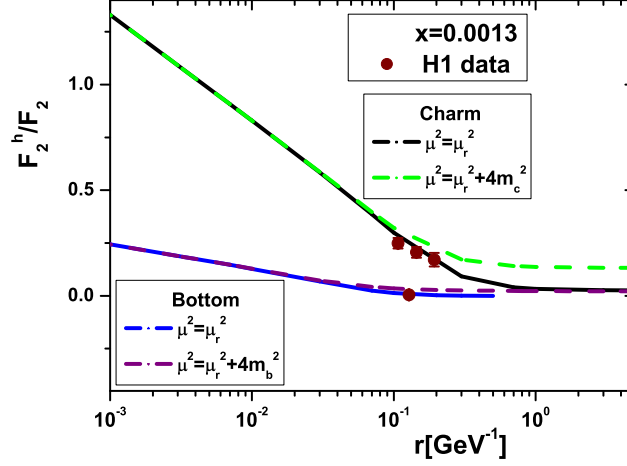


FIG. 9: Ratios F_2^c/F_2 and F_2^b/F_2 as functions of r with $\mu^2 = \mu_r^2$ and $\mu^2 = \mu_r^2 + 4m^2$ for $x=0.0013$. Experimental data are from the H1-Collaboration [51,54].

TABLE III: The ratios F_2^c/F_2 and F_2^b/F_2 with the renormalization and factorization scales are compared with the predictions of Ref.[7] from the BGK and IP-sat models.

x	Q^2 [GeV ²]	$\frac{F_2^c}{F_2} _{\text{IP-sat..BGK}}$	$\frac{F_2^b}{F_2} _{\text{IP-sat..BGK}}$	$\frac{F_2^c}{F_2} _{\mu_r^2.. \mu_r^2 + 4m^2}$	$\frac{F_2^b}{F_2} _{\mu_r^2.. \mu_r^2 + 4m^2}$
10^{-2}	5	0.096-0.100	0.00042-0.00044	0.072-0.156	<0.014
	10	0.144-0.149	0.00165-0.00168	0.133-0.196	0.00008-0.02150
	50	0.233-0.234	0.0115-0.0112	0.323-0.342	0.0151-0.0346
10^{-4}	5	0.150-0.154	0.0034-0.0033	0.080-0.165	0.0013-0.0274
	10	0.197-0.200	0.0060-0.0057	0.139-0.202	0.0031-0.0286
	50	0.280-0.280	0.0195-0.0186	0.328-0.346	0.0168-0.0367
10^{-6}	5	0.184-0.194	0.0057-0.0053	0.080-0.165	0.0014-0.0275
	10	0.230-0.238	0.0089-0.0086	0.139-0.202	0.0032-0.0287
	50	0.305-0.308	0.0244-0.0235	0.328-0.346	0.0168-0.0367

$x=0.0013$. In this figure, the ratio of the structure functions are compared with the H1 Collaboration data in Refs.[51] and [54]. The error bars of the ratio F_2^h/F_2 are determined by $\Delta(F_2^h/F_2) = F_2^h/F_2 \sqrt{(\Delta F_2^h/F_2^h)^2 + (\Delta F_2/F_2)^2}$, where ΔF_2^h and ΔF_2 are collected from the H1 experimental data in Refs.[51] and [54] respectively. The results obtained from the ratios are comparable to the H1 data [51,54]. Realistic values of F_2^c/F_2 can only range from zero to at most about 0.4 in the HERA energy range [38, 55]⁸. The results for the ratios F_2^c/F_2 and F_2^b/F_2 , in Fig.9, are predicted at low values of r according to the LHeC and FCC-he energy range and will be able to be considered in these collisions. In particular, the unphysical upper bound [38] $F_2^c/F_2 = 1$ will be obtained at the low value of r due to the FCC-he center-of-mass energy.

Recently, the structure functions F_2, F_L and heavy quark structure functions, F_2^c, F_2^b from the models BGK and

⁷ For further discussion please see Refs.[34,53]

⁸ The average value of the ratio F_2^c/F_2 is determined to be $\langle F_2^c/F_2 \rangle = 0.237 \pm 0.021^{+0.043}_{-0.039}$ in Ref.[56].

IP-sat are predicted⁹ in the range $(x, Q^2) : (10^{-6} - 10^{-2}, 5.0 - 50 \text{ GeV}^2)$ in Ref.[7]. We compared the ratios with the results of the BGK and IP-sat models in Table III. One shows in this table that our calculations are comparable with the predictions from the BGK and IP-sat models. We can see that the predictions from the BGK and IP-sat models lie between $(\mu_r^2 \lesssim \text{BGK, IP-sat} \lesssim \mu_r^2 + 4m^2)$ the bounds as the maximum is of the order $(\mu_r^2) - (\mu_r^2 + 4m^2)$. The differences between the results are due to the free-fit parameters of the models in Refs.[4] and [23].

IV. Conclusions

In this work we have computed the heavy quark structure functions $F_{2,L}^h, h = c, b, t$ within the k_t factorization framework, using unifying the color dipole picture and double asymptotic scaling approaches for the integrated gluon density using the GBW and BGK models at small Bjorken x values. We have first considered the structure functions $F_{2,L}^h$ in a wide range of the transverse separation r from the HERA to FCC-he center-of-mass energy. Then we have obtained bounds on F_L^h/F_2^h as well as a correlated bound on the ratios F_2^c/F_2 and F_2^b/F_2 as they are consistent with the experimental data from HERA collider at moderate and large r . It will be interesting to compare these bounds with future results from measurements of these structure functions as r decreases.

We achieved a good agreement between the HERA experimental data for the charm and bottom structure functions and our theoretical predictions with the renormalization and factorization scales. We demonstrated the importance of the contributions of F_L^c and F_L^b at small r in further colliders. For the top quark pair production, which will be one kind of important production channel at LHeC and FCC-he, the ratio of structure functions (i.e., R^t) is determined and compared with the charm and bottom ratios (i.e., R^c and R^b) at small r which are dominated by the center-of-mass energies in new colliders at the renormalization scale $\mu^2 = \mu_r^2 + 4m^2$. To estimate the uncertainties of our calculations, the standard variations in default scales (i.e., renormalization and factorization) are introduced. The uncertainty range of scales increases as r increases.

Additionally, effects of the Sudakov form factor were investigated for the heavy quark structure functions in a wide range of r . The Sudakov form factor modifies the heavy quark structure functions in the small region of r owing to the saturation effect. The effect is visible for a small value of r and disappears when r increases. Moreover, we compared our predictions of the ratio F_2^c/F_2 and F_2^b/F_2 with the BGK and IP-sat models at low values of x and found all good agreement with data sets in the intervals of the factorization and renormalization scales. We hope that this paper at low x and low r will be useful in future phenomenological studies of the heavy quark structure functions at future colliders such as EIC, LHeC and the FCC-he.

ACKNOWLEDGMENTS

The author is grateful to Razi University for the financial support of this project.

APPENDIX

In the high energy regime, defined by $x \ll 1$, the coefficient functions have the compact forms [34]

$$\begin{aligned}
 B_{2,g}^{(0)}(1, \xi_r) &= \frac{2}{3}[1 + 2(1 - \xi_r)J(\xi_r)], \\
 B_{L,g}^{(0)}(1, \xi_r) &= \frac{4}{3}x_2\{1 + 6\xi_r - 4\xi_r[1 + 3\xi_r]J(\xi_r)\}, \\
 B_{k,g}^{(1)}(x, \xi_r) &= \beta[R_{k,g}^{(1)}(1, \xi_r) + 4C_A^2 B_{k,g}^{(0)}(1, \xi_r)L_\mu], \\
 B_{k,g}^{(2)}(x, \xi_r) &= \beta\ln(1/x)[R_{k,g}^{(2)}(1, \xi_r) + 4C_A R_{k,g}^{(1)}(1, \xi_r)L_\mu + 8C_A^2 B_{k,g}^{(0)}(1, \xi_r)L_\mu^2],
 \end{aligned} \tag{30}$$

⁹ Within the color dipole approach, the impact parameter saturation model (IP-SAT) and the BGK model include DGLAP evolution as the gluon density is parametrized, in both models, at the initial scale Q_0^2 then scales μ^2 by using the LO or NLO evolution equations.

with

$$\begin{aligned}
R_{2,g}^{(2)}(1, \xi_r) &= \frac{32}{27} C_A^2 [46 + (71 - 92a)J(\xi_r) + 3(13 - 10\xi_r)I(\xi_r) - 9(1 - \xi_r)K(\xi_r)], \\
R_{L,g}^{(2)}(1, \xi_r) &= \frac{64}{27} C_A^2 x_2 \{34 + 240\xi_r - [3 + 136\xi_r + 480\xi_r^2]J(\xi_r) + 3[3 + 4\xi_r(1 - 6\xi_r)]I(\xi_r) + 18\xi_r(1 + 3\xi_r)K(\xi_r)\}, \\
R_{2,g}^{(1)}(1, \xi_r) &= \frac{8}{9} C_A [5 + (13 - 10\xi_r)J(\xi_r) + 6(1 - \xi_r)I(\xi_r)], \\
R_{L,g}^{(1)}(1, \xi_r) &= -\frac{16}{9} C_A x_2 \{1 - 12\xi_r - [3 + 4\xi_r(1 - 6\xi_r)]J(\xi_r) + 12\xi_r[1 + 3\xi_r]I(\xi_r)\},
\end{aligned} \tag{31}$$

where

$$\begin{aligned}
K(\xi_r) &= -\sqrt{x_2} [4(\zeta_3 + \text{Li}_3(-t) - \text{Li}_2(-t)\text{ln}t - 2S_{1,2}(-t)) + 2\text{ln}(\xi_r x_2)(\zeta_2 + 2\text{Li}_2(-t)) \\
&\quad - \frac{1}{3}\text{ln}^3 t - \text{ln}^2(\xi_r x_2)\text{ln}t + \text{ln}(\xi_r x_2)\text{ln}^2 t], \\
I(\xi_r) &= -\sqrt{x_2} [\zeta_2 + \frac{1}{2}\text{ln}^2 t - \text{ln}(\xi_r x_2)\text{ln}t + 2\text{Li}_2(-t)], \\
J(\xi_r) &= -\sqrt{x_2} \text{ln}t, \\
t &= \frac{1 - \sqrt{x_2}}{1 + \sqrt{x_2}}, \\
x_2 &= \frac{1}{1 + 4\xi_r}, \\
L_\mu &= \text{ln} \frac{4m_f^2}{\mu_r^2},
\end{aligned} \tag{32}$$

where

$$\begin{aligned}
\text{Li}_2(x) &= -\int_0^1 \frac{dy}{y} \text{ln}(1 - xy), \\
\text{Li}_3(x) &= -\int_0^1 \frac{dy}{y} \text{ln}(y) \text{ln}(1 - xy), \\
S_{1,2}(x) &= \frac{1}{2} \int_0^1 \frac{dy}{y} \text{ln}^2(1 - xy),
\end{aligned} \tag{33}$$

are the dilogarithmic function $\text{Li}_2(x)$, the trilogarithmic function $\text{Li}_3(x)$ and Nilsen Polylogarithm $S_{1,2}(x)$.

REFERENCES

1. V.N.Gribov, B.L.Ioffe, and I.Y.Pomeranchuk, Sov.J.Nucl.Phys. **2**, 549 (1966).
2. B.L.Ioffe, Phys.Lett.B **30**, 123 (1969).
3. J.J.Sakurai, Currents and Mesons, The University of Chicago Press, 1969.
4. D.Schildknecht, Acta Phys.Polon.B **37**, 595 (2006).
5. N.N.Nikolaev and B.G.Zakharov, Z.Phys.C **49**, 607 (1991); Z.Phys.C **53**, 331 (1992).
6. C.Ewerz, A.von Manteuffel and O.Nachtmann, J.High Energ.Phys. **03**, 102 (2010).
7. D.A.Fagundes and M.V.T.Machado, Phys.Rev.D **107**, 014004 (2023).
8. V.P.Goncalves and M.V.T.Machado, Phys.Rev.Lett.**91**, 202002 (2003).
9. E.Iancu, A.Leonidov and L.McLerran, Nucl.Phys.A **692**, 583 (2001); Phys.Lett.B **510**, 133 (2001).
10. E.Iancu,K.Itakura and S.Munier, Phys.Lett.B **590**, 199 (2004).
11. K.Kutak and A.M.Stasto, Eur.Phys.J.C **41**, 343 (2005).

12. N.N.Nikolaev and B.G.Zakharov, Phys.Lett.B **332**, 184 (1994); N. N. Nikolaev and W. Schäfer, Phys. Rev. D **74**, 014023 (2006).
13. V.S.Fadin, E.A.Kuraev and L.N.Lipatov, Phys.Lett.B **60**, 50(1975); L.N.Lipatov, Sov.J.Nucl.Phys. **23**, 338(1976); I.I.Balitsky and L.N.Lipatov, Sov.J.Nucl.Phys. **28**, 822(1978).
14. A.H.Mueller and B.Patel, Nucl.Phys.B **425**, 471 (1994).
15. R.S.Thorne, Phys.Rev.D **71**, 054024 (2005); M.A.Betemps and M.V.T.Machado, Eur.Phys.J.C **65**, 427 (2010).
16. R. D. Ball and S. Forte, Phys. Lett. B **335**, 77 (1994).
17. A.D.Bolognino, A.Szczurek and W. Schäfer, Phys.Rev.D **101**, 054041 (2020); A.D.Bolognino, F.G.Celiberto, D.Y.Ivanov, A. Papa, W. Schäfer and A. Szczurek, Eur. Phys.J.C **81**, 846 (2021); A.D.Bolognino, F.G.Celiberto, D.Y.Ivanov and A. Papa, Eur. Phys.J.C **78**, 1023 (2018); A.D.Bolognino, F.G.Celiberto, M.Fucilla, Dmitry Yu. Ivanov, A.Papa, W.Schäfer and A.Szczurek, International Conference on Hadron Spectroscopy and Structure in memoriam Simon Eidelman (HADRON2021), (2021).
18. I.P.Ivanov and N.N.Nikolaev, Phys.Rev.D **65**, 054004 (2002).
19. M.A.Kimber, J.Kwiecinski, A.D.Martin and A.M.Stasto, Phys.Rev.D **62**, 094006 (2000).
20. T.Goda, K.Kutak and S.Sapeta, Nucl.Phys.B **990**, 116155 (2023).
21. M.A.Kimber, A.D.Martin and M.G.Ryskin, Eur.Phys.J.C **12**, 655 (2000).
22. B.W.Xiao, F.Yuan and J.Zhou, Nucl.Phys.B **921**, 104 (2017).
23. K. Golec-Biernat and S.Sapeta, J.High Energ. Phys. **03**, 102 (2018).
24. LHeC Collaboration and FCC-he Study Group, P. Agostini et al., J. Phys. G: Nucl. Part. Phys. **48**, 110501(2021).
25. E. Laenen et al., Phys. Lett. B **291**, 325 (1992); E. Laenen et al., Nucl. Phys. B **392**, 162 (1993); S. Riemersma, J. Smith, W.L. van Neerven, Phys. Lett. B **347**, 143 (1995); S. Alekhin et al., Phys. Rev. D **81**, 014032 (2010); S. Alekhin and S. Moch, Proc. of DIS2011, (2011); S. Alekhin, J. Blümlein, S. Moch, Phys. Rev. D **86**, 054009 (2012); S. Alekhin et al., Phys. Rev. D **96**, 014011 (2017); S. Alekhin, J. Blümlein, S. Klein and S. Moch, Proc. of DIS2009, (2009); M. Glück et al., Phys. Lett. B **664**, 133 (2008); H.L. Lai et al., Phys. Rev. D **82**, 074024 (2010); A.D. Martin et al., Eur. Phys. J. C **70**, 51 (2010); S. Alekhin and S. Moch, Phys. Lett. B **699**, 345 (2011).
26. S. Forte et al., Nucl. Phys. B **834**, 116 (2010); R.D. Ball et al. [NNPDF Collaboration], Nucl. Phys. B **849**, 296 (2011); R.D. Ball et al. [NNPDF Collaboration], Nucl. Phys. B **855**, 153 (2012); R.D. Ball et al. Eur.Phys.J.C **78**, 321 (2018).
27. R.Thorne, Phys.Rev.D **73**, 054019 (2006); R.Thorne, Phys.Rev.D **86**, 074017 (2012).
28. R.S.Thorne, DIS1998, (1998); A.D.Martin W.J.Stirling and R.S.Thorne, Phys.Lett.B **636**, 259(2006).
29. J.Blümlein, A.De Freitas, C.Schneider and K.Schönwald, Phys. Lett.B **782**, 362(2018).
30. S.Alekhin, J. Blümlein and S. Moch, Phys. Rev. D **102**, 054014 (2020).
31. A.V.Kotikov and G.Parente, Nucl.Phys.B **549**, 242 (1999).
32. A.Yu.Illarionov, A.V.Kotikov and G.Parente, Phys.Part.Nucl. **39**, 307 (2008).
33. L.Mankiewicz, A.Saalfeld and T.Weigl, Phys.Lett.B **393**, 175 (1997).
34. A.V.Kotikov, A.V.Lipatov and P.Zhang, Phys.Rev.D **104**, 054042 (2021).
35. G.R.Boroun and B.Rezaei, arXiv[hep-ph]:2309.04832 (will be appear in EPJA).
36. G.Beuf, T.Lappi and R.Paatelainen, Phys.Rev.D **104**, 056032 (2021).
37. G.Beuf, Phys.Rev.D **85**, 034039 (2012).
38. C.Ewerz, A.von Manteuffel and O.Nachtmann, Phys.Rev.D **77**, 074022 (2008); M.Niedziela and M.Praszalowicz, Acta Physica Polonica B **46**, 2018 (2015).
39. C.Ewerz, A.von Manteuffel, O.Nachtmann and A.Schoning, Phys. Lett.B **720**, 181 (2013); C.Ewerz and O.Nachtmann, Phys.Lett.B **648**, 279 (2007).
40. B.Rezaei and G.R.Boroun, Phys.Rev.C **101**, 045202 (2020); G.R.Boroun and B.Rezaei, Phys.Rev.C **103**, 065202 (2021); Phys.Letts.B **816**, 136274 (2021).
41. G.R.Boroun, Eur.Phys.J.A **57**, 219 (2021).
42. M.Klein, arXiv:1802.04317; M.Klein, Ann.Phys.**528**, 138(2016).
43. G.R.Boroun, M.Kuroda and D.Schildknecht, arXiv: 2206.05672.
44. M.Kuroda and D.Schildknecht, Phys.Rev. D **96**, 094013 (2017); Phys.Rev. D **85**, 094001 (2012); Int. J. Mod. Phys. A **31**, 1650157 (2016).
45. LHC Higgs Cross Section Working Group collaboration, CERN Yellow Reports: Monographs Volume 2/2017 (CERN-2017-002-M).
46. NNPDF Collaboration (Ball R. D. et al.), Eur.Phys.J.C **77**, 663 (2017).
47. S.Zarrin and S.Dadfar, Phys.Rev.D **106**, 094007 (2022).
48. J. Lan et al., Phys. Rev. D **102**, 014020 (2020).

49. H. Khanpour, Nucl.Phys.B **958**, 115141 (2020).
50. G.R.Boroun, Chinese Physics C **45**, 063105 (2021); Eur.Phys.J.Plus **138**, 252 (2023); Phys.Letts.B **838**, 137712 (2023).
51. F.D.Aaron et al. (H1 Collaboration), Eur.Phys.J.C **65**, 89 (2010).
52. N.N.Nikolaev and V.R.Zoller, Phys.Atom.Nucl **73**, 672 (2010); N.N.Nikolaev, J.Speth and V.R.Zoller, Phys.Lett.B **473**, 157 (2000); R.Fiore, N.N.Nikolaev and V.R.Zoller, JETP Lett **90**, 319 (2009); A.Y.Illarionov and A.V.Kotikov, Phys.Atom.Nucl. **75**, 1234 (2012) ; N.Ya.Ivanov and B.A.Kniehl, Eur.Phys.J.C **59**, 647 (2009); N.Ya.Ivanov, Nucl.Phys.B **814**, 142(2009); J.Blumlein et al., Nucl.Phys.B **755**, 272 (2006); A.V.Kotikov, arXiv[hep-ph]: 1212.3733; G.R.Boroun and B.Rezaei, Int.J.Mod.Phys.E **24**, 1550063 (2015); G.R.Boroun and B.Rezaei, Nucl.Phys.A **929**, 119 (2014); G.R.Boroun, Eur. Phys. J. Plus **137**, 1212 (2022).
53. N.A.Abdulov, A.V.Kotikov and A.V.Lipatov, JETP Lett. **117**, 401 (2023).
54. C.Adloff et al. (H1 Collaboration), Eur.Phys.J.C **21**, 33 (2001).
55. G.R.Boroun and B.Rezaei, EPL **133**, 61002 (2021).
56. C. Adloff et al. (H1 Collaboration), Z.Phys.C **72**, 593 (1996).